Application of airborne LiDAR data and airborne multispectral imagery to structural mapping of the upper section of the Troodos ophiolite, Cyprus

Stephen Grebby[a,*], Dickson Cunningham[a], Jonathan Naden[b], Kevin Tansey[c]

[a]*Department of Geology, University of Leicester, University Road, Leicester LE1 7RH, UK*

[b]*British Geological Survey, Keyworth, Nottingham NG12 5GG, UK*

[c]*Department of Geography, University of Leicester, University Road, Leicester LE1 7RH, UK*

[*]Corresponding author. Tel: +44 (0)116 252 3922

Fax: +44 (0)116 252 3918

Email address: srg11@le.ac.uk

Abstract Structural maps are traditionally produced by mapping features such as faults, folds, fabrics, fractures and joints in the field. However, large map areas and the spatially limited ground perspective of the field geologist leads to the inevitability that some important geological features may go un-noticed. The ability to recognise and map both local and regional structural features using high-resolution remote sensing data provides an opportunity to complement field-based mapping to enable the generation of more comprehensive structural maps. Nonetheless, vegetation cover can adversely affect the extraction of structural information from remotely sensed data as it can mask the appearance of subtle spectral and geomorphological features that correspond to geological structures. This study investigates the utility of airborne Light Detection

And Ranging (LiDAR) data and airborne multispectral imagery for detailed structural mapping in vegetated ophiolitic rocks and sedimentary cover of a section of the northern Troodos ophiolite, Cyprus. Visual enhancement techniques were applied to a 4 m airborne LiDAR digital terrain model and 4 m airborne multispectral imagery to assist the generation of structural lineament maps. Despite widespread vegetation cover, dykes and faults were recognisable as lineaments in both datasets and the predominant strike trends of lineaments in all resulting maps were found to be in agreement with field-based structural data. Interestingly, prior to fieldwork, most lineaments were assumed to be faults, but were ground verified as dykes instead, emphasising the importance of ground truthing. The dyke and fault trends documented in this study define a pervasive structural fabric in the upper Troodos ophiolite that reflects the original sea-floor spreading history in the Larnaca graben. This structural fabric has not previously been observed in such detail and is likely to be continuous in adjacent regions under sedimentary cover. This information may be useful to future exploration efforts in the region focused on identification of structurally controlled mineral and groundwater resources. Overall, our case study highlights the efficacy of airborne LiDAR data and airborne multispectral imagery for extracting detailed and accurate structural information in hard-rock terrain to help complement field-based mapping.

Keywords: Troodos ophiolite; airborne LiDAR; multispectral imagery; structural mapping

Introduction

In regions that have been deformed, documenting the structural geology is a key objective of geological mapping (Barnes and Lisle 2004). Geological maps portraying structural features are important because they provide valuable information for understanding the local crustal architecture and deformation history. In addition, structural maps may inform seismic and landslide hazard assessments, and provide useful information for major engineering projects and the exploration of groundwater, petroleum and mineral resources (Moore and Waltz 1983; Kresic 1995; Karnieli et al. 1996; Wladis 1999; Harris et al. 2001; Peña and Abdelsalam 2006; Corgne et al. 2010).

Traditionally, structural maps are produced by mapping features such as faults, folds, fabrics, fractures and joints in the field. Although arguably the most reliable and accurate maps are those produced using this approach, large map areas, time constraints and the limited ground perspective of the field geologist has the potential to increase the possibility that not all structural features will be identified (Süzen and Toprak 1998). However, the ability to also recognise and map structural features using remote sensing data offers the potential to provide complementary information and the opportunity to generate more comprehensive and accurate structural maps.

Many important structural features (e.g., faults, fractures, veins, dykes, joints) may be expressed as lineaments in remotely sensed imagery and digital elevation models (DEMs; Masoud and Koike 2006). This is particularly the case with steep structures because their surface traces are less deflected and curved across uneven topography. A lineament is defined by O'Leary et al. (1976) as "a mappable, simple or composite linear feature of a surface, whose parts are aligned in a rectilinear or slightly curvilinear relationship and which differs distinctly from the patterns of adjacent features and presumably reflects a subsurface phenomenon". In spectral imagery, lineaments are typically recognised as edges defined by a series of adjacent pixels at the boundary of brightness changes (Koike et al. 1998). Such spectral features may correspond to variations in surface composition or shadowing. In the context of the topographic domain, geological lineaments are typically associated with geomorphological features such as linear valleys, ridgelines, escarpments and slope breaks (Jordan and Schott 2005). Such features are also expressed as edges in DEMs, defined either by an abrupt change in elevation (i.e., slope break) or by an increase or decrease in elevation for a short lateral distance (i.e., ridgelines and valleys).

Lineaments observed in remotely sensed data products that are interpreted to be geological structures are typically manually traced. However, this technique can be time-consuming and tedious at regional mapping scales, and also highly subjective and therefore irreproducible (Masoud and Koike 2006). A variety of enhancement techniques are commonly used to try to improve the efficiency and objectivity of the visual interpretation and mapping process. Principal Component Analysis, decorrelation stretching and generation of false-colour composite images are useful techniques for exaggerating subtle colour or brightness differences in spectral imagery to accentuate the appearance of potential lineaments (Qari 1991; Mountrakis et al. 1998). Shaded relief models generated from DEMs are a powerful tool for enhancing the appearance of lineaments in topographic data. This is because the artificial solar illumination azimuth and inclination angles can be varied to help identify lineaments in a range of orientations by recognising the shadowing effects (manifest as boundaries between light and dark tones) caused by abrupt changes in elevation (Jordan and

Schott 2005). Additional techniques that are commonly applied to spectral imagery and DEMs in order to enhance the visual appearance of edges include convolution filters, such as Sobel, Prewitt and Laplacian filters (Moore and Waltz 1983; Süzen and Toprak 1998; Wladis 1999), and morphological operators, such as erosion, dilation, opening and closing (Tripathi et al. 2000; Ricchetti and Palombella 2005).

Automated algorithms for mapping geological lineaments from remotely sensed data have also received considerable attention (Argialas and Mavrantza 2004). Examples include algorithms based on Canny edge detection (Corgne et al. 2010), the Hough transform (Karnieli et al. 1996; Fitton and Cox 1998), line-tracing (Koike et al. 1995) and morphometric feature parameterisation (Wallace et al. 2006). Despite increasing the reproducibility, efficiency and objectivity of lineament mapping, there are concerns regarding the suitability of automated algorithms for geological lineament detection (Parsons and Yearley 1986) — the most obvious being their inability to differentiate geological lineaments from non-geological lineaments (e.g., roads, field boundaries). Therefore, for reasonably sized areas, the task of lineament mapping is arguably best performed manually based on human perception.

Vegetation cover can have somewhat adverse effects on the extraction of structural information from remotely sensed data because vegetation, especially tall dense vegetation (e.g., forests), is capable of masking the appearance of subtle spectral and geomorphological lineaments that correspond to geological structures. Also, with only moderate spatial resolution (~ 15–30 m), the utility of data acquired from classic spaceborne instruments — such as Landsat TM and the Shuttle Radar Topographic Mission (SRTM) — is generally confined to the identification of only regional structural features. The use of high-resolution (ca.

1–4 m) airborne Light Detection And Ranging (LiDAR) data and airborne spectral imagery can enhance the utility of remote sensing for structural mapping because these datasets enable the extraction of detailed information about both local and regional geological structures. Furthermore, with the capability to acquire accurate and high-resolution topographic data even in forested terrain (Kraus and Pfeifer 1998), airborne LiDAR is now established as an important tool for mapping the surface traces of regionally-significant faults in either vegetated or non-vegetated terrain (e.g., Harding and Berghoff 2000; Haugerud et al. 2003; Prentice et al. 2003; Cunningham et al. 2006; Arrowsmith and Zielke 2009). Nevertheless, with the exception of a few studies which examine the use of airborne LiDAR for identifying bedrock structures (Wallace et al. 2006; Nyborg et al. 2007; Pavlis and Bruhn 2011), the broader utility of airborne LiDAR for structural applications has yet to be fully realised.

The objective of this study is to investigate the utility of airborne LiDAR data and airborne multispectral imagery for detailed structural mapping of the vegetated ophiolitic rocks and sedimentary cover in a section of the upper Troodos ophiolite, Cyprus. Owing primarily to the reliability concerns associated with automated algorithms, the efficacy of airborne LiDAR data and airborne multispectral imagery for structural mapping is evaluated here by manually generating lineament maps with the aid of several visual enhancement techniques. Structural information extracted from the data is subsequently validated using field-based data.

Geological setting

The Troodos ophiolite is an uplifted slice of oceanic crust and lithospheric mantle that was created through sea-floor spreading (Gass 1968; Moores and Vine 1971). The ophiolite forms a dome-like structure centred on Mt. Olympus (1,952 m) that dominates the geology and topography of the island of Cyprus. Stratigraphically, the ophiolite comprises a mantle sequence of harzburgites, dunites and a serpentinite diapir, a largely gabbroic plutonic complex, a sheeted dyke complex, a lava sequence and oceanic sediments at decreasing elevations along the northern slopes of the range (Varga and Moores 1985). The study area is situated on the contact between the lava sequence and overlying sedimentary cover sequences in the northern foothills of the Troodos ophiolite (Fig. 1a). It covers approximately 16 km^2 and contains four main lithological units — the Basal Group (generally comprising 80–90% dykes and 10–20% lavas), Pillow Lavas (Upper and Lower), late Cretaceous to early Miocene chalky marls of the Lefkara Formation and alluvium–colluvium. This area is located in the most eastern of three structural grabens (the Larnaca graben) proposed and interpreted by Varga and Moores (1985) as fossil axial valleys of an eastward migrating spreading centre in the northern part of the ophiolite. Faulting within this area is dominated by a NW–SE trend, which is parallel to the interpreted spreading axis of the Larnaca graben and is therefore consistent with the proposed crustal extension in this region. Moreover, the dominant dyke trend in the study area is parallel to this NW–SE faulting trend (Gass 1960). A less significant N–S structural trend observed in this region is believed to correspond to a later stage of normal faulting (Gass 1960; Boyle and Robertson 1984).

Ubiquitous vegetation typically covering between 30–90% of the surface area is responsible for a lack of completely exposed outcrops in the study area. Vegetation cover type generally varies from moderate-to-dense lichen cover, to crops (e.g., cereals, olive groves) as well as both green and dry grasses, to what can be broadly described as garrigue or maquis, predominantly comprising scrubby short dry grasses, short-to-medium height shrubs and scattered small trees. Other types of mostly sporadic vegetation cover occurring throughout the study area include trees — ranging from isolated trees (e.g., pines and oaks) to dense thickets and copses — and areas covered by tall, dry grasses and scrubland.

Remote sensing data

Airborne LiDAR data and Airborne Thematic Mapper (ATM) multispectral imagery were acquired over the Troodos study area in May 2005 by the Natural Environment Research Council Airborne Research and Survey Facility. The airborne LiDAR data were acquired at an average flying altitude of 2550 m using an ALTM-3033 system operating with a laser pulse repetition rate of 33 kHz and a half-scan angle of ±19.4° either side of the nadir. The resulting dataset contains point data from five overlapping flight-lines, each with a swath width of 1400–1500 m and an overlap of 20%–50% between adjacent swaths. After initial pre-processing by the Unit for Landscape Modelling at the University of Cambridge, UK, the airborne LiDAR point data were delivered as ASCII files containing the x-y-z coordinates of all first and last returns in the WGS84 Universal Transverse Mercator (UTM) zone 36-North coordinate system. On delivery, the point data were classified as either ground or non-ground returns (e.g., trees, buildings) using the triangulated irregular network densification algorithm (Axelsson 2000) implemented in the TerraScan software (Terrasolid Ltd., Finland). Points corresponding to non-ground returns were subsequently discarded, whilst those classified as ground returns were interpolated using a block kriging algorithm in order to generate a 4 m digital terrain model (DTM) or "bare-earth" DEM (Fig. 1b). A more detailed description of the airborne LiDAR data processing steps is provided by Grebby et al. (2010).

The ATM imagery initially comprised 11 spectral bands located in the visible/near-infrared (VNIR; Bands 1–8), short-wave infrared (SWIR; Bands 9–10) and thermal infrared (TIR; Band 11) regions of the electromagnetic spectrum. However, due to data quality concerns, and for the purpose of concentrating solely on reflectance data, ATM Bands 1 and 11 were omitted from any further analysis. Five northwest-southeast trending flight-lines of imagery were acquired over the study area and delivered as Level 1b Hierarchical Data Format (HDF) files, with radiometric calibration algorithms applied and aircraft navigation information appended. The radiometric calibration involves conversion of the raw ATM data to at-sensor radiance units, followed by scaling to 16-bit digital numbers (DNs). Conversion of the raw ATM data to at-sensor radiance is achieved by applying gains and offsets — determining using a source traceable to a national standard — to the data recorded in each of the wavebands (Hill et al. 2010). All image strips were individually geocorrected and re-sampled to a spatial resolution of 4 m using the AZGCORR software (Azimuth Systems) in conjunction with a 4 m airborne LiDAR DEM. The five geocorrected images were then corrected for limb-brightening, mosaicked and co-registered to the 4 m LiDAR DTM using ENVI 4.3 (ITT Visual Information Solutions, Boulder, Colorado) to generate the 4 m ATM imagery comprising Bands 2–10 (Fig. 1c). The reader is referred to Grebby et al. (2011) for further information regarding the processing steps applied to the ATM imagery.

Methods

The methodology employed in this study comprises four main steps: a preliminary analysis, followed by lineament enhancement, mapping and analysis and field validation. Each of these steps is discussed in detail below.

Preliminary analysis

A preliminary analysis was first undertaken to determine whether the main structural features in the study area could be identified using both the 4 m airborne LiDAR DTM and 4 m ATM imagery. The main structural features found in the Troodos study area are faults and dykes (Figs. 2 and 3). The locations of typical examples of a fault and a dyke were identified and cross-sectional profiles were extracted for these from the airborne LiDAR DTM and ATM imagery for inspection in order to determine the utility of the datasets for mapping the ophiolite structure.

The example fault (labelled “A” in Fig. 1b, c) is of a major fault located along a stream transect, which forms a cleft that cuts both sides of a canyon that contains the stream (Fig. 4a). Cross-sectional profiles extracted from the airborne LiDAR DTM and ATM imagery in the locality of this fault are shown in Figs. 4b and 4c, respectively. The fault can be clearly recognised in the LiDAR DTM profile as a decrease in elevation of approximately 0.5 m over a relatively short width of 7 m; forming a linear trough. This fault is also visible in the ATM imagery, albeit as a subtle decrease in brightness (or radiance) with edges defined by relatively abrupt changes in the brightness gradient at both boundaries.

The example dyke (labelled “B” in Fig. 1b, c) is located upstream (southwest) of the example fault. The dyke (or possibly a set of dykes) can be seen cutting across the stream to form an upstanding linear ridge feature in Pillow Lavas on the western bank of the stream (Fig. 4d). Cross-sectional profiles extracted from the airborne LiDAR DTM and ATM imagery in the locality of the dyke are shown in Figs. 4e and 4f, respectively. The dyke is clearly recognised as a 3 m wide ridgeline in the LiDAR DTM profile, bounded by abrupt decreases in elevation at both edges. Although the dyke can be identified in the ATM image profile as well, its expression is less conspicuous because of the narrower (~1 m) width of the feature. Nevertheless, the dyke is defined by boundaries caused by abrupt changes in the radiance gradient. Illumination conditions during image acquisition or smoothing effects during processing of the imagery could be responsible for the relatively narrow appearance of this particular dyke in the ATM imagery.

Lineament enhancement

It is apparent from the results of the preliminary analysis that both airborne remote sensing datasets are capable of revealing faults and dykes in the uppermost section of the Troodos ophiolite as lineaments. Accordingly, several visual enhancement techniques were applied to the airborne LiDAR DTM and ATM imagery to help generate structural lineament maps for the study area. However, prior to this, Principal Component Analysis (PCA) was first applied to the ATM imagery in order to reduce the number of spectral bands whilst still retaining most of the spectral information contained within the entire dataset. In addition to reducing data dimensionality, the PCA technique is also useful because it enhances spectral information by decorrelating the spectral data in all bands and can be used to segregate noise (Jensen 2005). An examination of the eigenvalues associated with the resulting nine ATM Principal Component (PC) bands revealed that the first three PC bands accounted for 97.5% of the total data variance (Table 1). Consequently, the first three PC bands were selected to represent the ATM imagery in further analysis, whereas the six remaining PC bands were discarded.

Shaded relief models

Shaded relief models — such as that shown in Fig. 1b — are topographic images that simulate the reflection of artificial light that is incident upon the surface from a user-specified inclination and azimuth. They are generated from DEMs by assigning shades of grey to pixels to represent their reflectance, which is usually calculated from the angle at which light is incident upon the terrain using a Lambertian reflection model (Masoud and Koike 2006). The ability to alter the shading effects by varying the illumination inclination and azimuth angles makes shaded relief models a powerful tool for identifying lineaments in a range of orientations. Here, a series of eight shaded relief models were generated from the airborne LiDAR DTM for azimuth illumination intervals of 45° (e.g., N, NE, E, etc.) and then visually interpreted to produce a lineament map. At each azimuth interval, the illumination inclination angle and the vertical exaggeration of the topographic surface were also systematically varied to try to help reveal as many lineaments as possible.

False-colour composite

In order to help identify lineaments using the ATM imagery, a false-colour composite (FCC) image was generated using ENVI 4.3 by assigning the ATM PC Bands 1, 2 and 3 to the red, green and blue channels of the computer monitor, respectively. As a result, subtle variations in the spectral properties of surface materials are typically enhanced in the FCC image through an increase in the colour contrast. Lineaments are then more readily identifiable in the FCC image as linear edges defined by sharp colour differences. A lineament map was therefore produced by visually interpreting the ATM PC FCC.

Laplacian filtering

Laplacian filters are a type of convolution filter commonly applied to remote sensing data for lineament mapping applications (Saha et al. 2002; Ali and Pirasteh 2004; Ricchetti and Palombella 2005). These filters are second derivative edge enhancement filters that operate without regard to edge orientation, i.e., they are non-directional. A Laplacian filter was applied to the airborne LiDAR DTM and each of the three ATM PC bands using a 3 × 3 pixel kernel with a weighting structure such as that shown in Fig. 5. In each case, the filtered image was added back to the original image at a ratio of 9:1 in order to improve the overall image interpretability. Two separate lineament maps were then produced by visually interpreting the filtered LiDAR DTM in addition to a FCC generated from the three filtered ATM PC bands.

Morphological transformation

Mathematical morphological operations such as dilation, erosion, opening and closing have also been applied to enhance lineaments in remotely sensed data. One of the most popular morphological techniques for edge detection is the Top Hat transformation (Tripathi et al. 2000; Ricchetti and Palombella 2005). The Top Hat transformation involves closing or opening operations followed by subtraction with the original image:

$$\text{Top Hat}(f) = f^{B} - f \qquad (1)$$

$$\text{Top Hat}(f) = f - f_{B} \qquad (2)$$

where f is the original image, f^{B} is the image obtained following the closing operation and f_{B} is the image obtained after the opening operation. The Top Hat transformation which involves the closing operation (that described by Eq. 1) is considered to yield better results for the extraction of structural features such as faults and fractures (Tripathi et al. 2000). Therefore, the closing-based Top Hat transformation was applied to the airborne LiDAR DTM and each of the ATM PC bands using a 3 × 3 pixel kernel with a weighting of 1 assigned to all elements — a weighting structure such as this avoids introducing directional bias. Again, two separate lineament maps were produced by visually interpreting the Top Hat-transformed LiDAR DTM as well as a FCC generated from the three Top Hat-transformed ATM PC bands.

Lineament mapping

A standard approach was adopted in an attempt to maximise both the consistency and objectivity of the visual mapping of lineaments. This involved producing all lineament maps using the ENVI 4.3 software via the following protocol. All enhanced image products were individually displayed in two image windows; one providing a regional perspective (1× zoom) and a second window providing more detailed view (2–4× zoom). Next, each image product was divided into four smaller, equally-sized sections so that each section could be individually examined to help ensure that the entire study area was subjected to a near-uniform visual examination (Parsons and Yearley 1986). Each of these sections was systematically examined for lineaments. Potential lineaments were inspected in order to establish their origin, and those interpreted to be of a geological nature were traced on-screen as line vectors using the overlay tool in the ENVI 4.3 software. The criteria used to determine the length and origin of all lineaments within a single image product and between products was kept constant. Such consistency helps to further reduce the subjectivity of the manual lineament mapping process. Following interpretation, line vectors associated with each image enhancement technique were exported as Shapefiles for subsequent interrogation.

Lineament analysis and validation

Lineament maps generated using the above procedure were analysed to evaluate the utility of the airborne LiDAR data and ATM imagery for structural mapping. To do this, the lineament orientations and lengths were extracted from each map by interrogating the Shapefiles in ArcMap (ArcGIS 9.2; ESRI, Redlands, California). Dominant structural trends expressed in the enhanced data products were revealed by plotting the orientation information on rose diagrams using the Stereonet/StereoWin software (http://www.geo.cornell.edu/geology/faculty/RWA/programs/). A variety of statistics relating to the numbers and lengths of lineaments were also computed. The spatial distribution of lineaments in the maps were analysed by way of lineament density maps derived using the Spatial Analyst Line Density tool in the ArcMap Toolbox for a search radius of 250 m.

A field survey was undertaken to collect structural measurements for the purpose of validating the results of the airborne LiDAR- and ATM-based lineament mapping. The field survey was conducted by measuring the strike and dip of faults and dykes encountered along the transect highlighted in Fig. 1b, c. This transect — which predominantly comprises a stream transect — provides excellent exposure and runs perpendicular to the apparent NW–SE structural trend in the study area. Structural information obtained along this transect and in the adjacent hills should therefore reflect the primary regional structural trends, thus removing the requirement of an extensive study area-wide field survey for validation. During the field survey, only faults extending beyond the local drainage were measured since very minor faults were not anticipated to be detectable in the remotely sensed data products. Field-based structural measurements were plotted on stereonets and rose diagrams (again using Stereonet/StereoWin software) to enable comparison with remote sensing-based lineament data.

Results and discussion

Field-based structural data

Field-based strike and dip measurements of faults and dykes exposed along the 4 km transect enable the most prominent structural trends within the study area to be determined. In the field, individual dykes and less abundant multiple dyke sets were predominantly observed striking NW–SE and dipping steeply towards the NE (Fig. 6a). This is consistent with other observations concerning the attitude of dykes which were made during mapping of the same region (Gass 1960). The average strike orientation for the 64 dykes is computed as 318° with relatively little deviation. Nevertheless, minor secondary N–S and E–W trends are apparent. The dip angle was found to vary between 42° and 90°, with an average dip of approximately 70° NE. Conversely, brittle faults do not appear to exhibit a clear dominant trend (Fig. 6b), although the majority of those observed strike between E–W and NW–SE. Dip angles for the field-mapped faults coincide with those of dykes; varying between 40–90° with an average of ~70°. The dip direction associated with the faults is also variable, with the majority dipping NE. When combined, the field-based structural data for dykes and faults reveals a dominant NW–SE trend within the study area (Fig. 6c). This dominant trend — comprising an average strike of 320° — is primarily dictated by the abundance of NW–SE striking dykes. Minor trends striking E–W and approximately N–S are also apparent in the combined field-based structural data. During fieldwork it became apparent that many of the lineaments previously identified in the remotely sensed data are dykes and not faults. This was a surprising result — we incorrectly expected that dykes would be somewhat less abundant in the uppermost Troodos ophiolitic crust (Basal Group and Pillow Lava sequences) and that major linear structures would be extensional faults. The dykes typically have margin-parallel fractures and are generally upstanding, although in some cases they were observed as eroded-out troughs depending on the rock types they intrude.

A major E–W ridge is visible in the remotely sensed data at the western end of the transect and was therefore ground-checked (location C in Fig. 1b, c). This ridge consists of a 285° trending dyke swarm with silicified and sheared dyke margins and parallel fault surfaces (Fig. 3b). Sub-horizontal slickenlines on polished and sheared surfaces indicate a strike-slip history and adjacent brecciated Pillow Lavas indicate intense brittle deformation. This is the most obvious fault zone in the study area. It was assumed to be a dyke prior to field verification because of its positive relief. However, unlike other faults within the study area, this zone is silicified and parallel to a major dyke set and thus erosionally resistant and ridge-forming. Since dykes are not necessarily ridge-forming lineaments and faults are not necessarily erosionally lowered linear troughs, we again emphasise that the follow-on fieldwork was essential for identifying the structural identity of lineaments identified in the remote sensing analysis.

Airborne LiDAR- and ATM-based lineament mapping

The six lineament maps and associated rose diagrams produced through the visual interpretation of the enhanced airborne LiDAR DTM and ATM products are shown in Fig. 7. An initial inspection reveals that the dominant NW–SE structural trend observable in the field is also apparent in all six lineament maps. Moreover, the overall spatial coverage of the lineaments is similar for all six maps. The vast majority of lineaments, which most likely correspond to dykes, are confined to the SE sector of the study area with a noticeable lack of lineaments in the NW and the extreme NE corner. The abundance of lineaments in the SE sector is unsurprising because this area is dominated by the Pillow Lava and Basal Group units in which dykes occur. Widespread alluvial–colluvial cover in the NW and Lefkara Formation outcrops in the NE corner explain the lack of lineaments in those areas because these younger cover sediments postdate the magmatic and tectonic events responsible for dyke emplacement and normal faulting.

Rose diagrams for all six lineament maps reveal a dominant NW–SE trend for the study area (Fig. 7). This result is corroborated by the field-based structural measurements shown in the Fig. 6c. Several minor secondary trends are also evident in a number of lineament maps; particularly those generated using the Top Hat-transformed LiDAR DTM (Fig. 7c) and Top Hat-transformed ATM PC FCC (Fig. 7d). Of these, the N–S and E–W trends are substantiated by the field measurements. Average lineament orientations are fairly consistent between maps, ranging from approximately 313° for the LiDAR shaded relief model (Fig. 7a) to 318° for the Top Hat-transformed LiDAR DTM (Fig. 7c). These average orientations are also comparable to that obtained from the field-based data. Accordingly, it is evident that both the airborne LiDAR and ATM data products are useful tools for revealing the dominant dyke and faulting trends of the Troodos ophiolite.

Despite only minor differences in the orientation information for the various enhancement techniques, further interrogation of the lineament maps reveals some notable differences relating to the abundance and lengths of lineaments (Table 2). A maximum number of 316 lineaments were identified using the Laplacian-filtered LiDAR DTM, compared to an average of 213 for the five other enhanced products. With regards to the two data types, the ATM-based enhancement techniques resulted in the identification of 15% more lineaments on average than LiDAR DTM-based techniques, with the exception of the Laplacian-filtered LiDAR DTM. This suggests that lineaments are generally more noticeable in ATM-derived colour composite images than in the greyscale LiDAR DTM products. Nevertheless, the high abundance of lineaments recognised using the Laplacian-filtered DTM could be an indication that this is the most superior technique for enhancing the appearance of lineaments in the airborne LiDAR DTM.

Frequency distributions of lineament lengths associated with each enhancement technique are shown in Fig. 8. All distributions appear unimodal and are positively skewed due to a profusion of lineaments with lengths ranging between 50–400 m. The Laplacian-filtered LiDAR DTM is associated with the greatest abundance of short lineaments, and is responsible for both the shortest mapped lineament (38.2 m) and the shortest average lineament length (158.4 m). This, together with the high number of lineaments associated with this enhancement technique, initially suggests that longer lineaments appear segmented in the Laplacian-filtered LiDAR DTM, therefore resulting in shorter but more numerous lineaments. However, evidence of lineament segmentation is not apparent in the Laplacian-filtered LiDAR DTM and the total lineament length is at least 10% longer than for any other technique, indicating that the additional lineaments do not simply arise through the division of lineaments that appear longer in the other enhanced data products.

The lineament density maps shown in Fig. 9 reveal the spatial distribution of the lineaments mapped using each of the enhancement techniques. As might be expected due partly to the similarities in the spatial coverage of lineaments in all six maps, the ensuing lineament density maps are also visibly similar. The highest densities are commonly observed in the east of the study area, within the Pillow Lavas (see Fig. 1a). In several maps, smaller regions of high lineament density are also observed towards the NE and slightly due south of the centre, again coinciding with the outcropping of Pillow Lavas. Considering that the field-based data indicates that the vast majority of lineaments in the study area are dykes together with the geological definitions of the Basal Group and Pillow Lava units (e.g., Bear 1960), one would expect the highest lineament densities to be associated with the Basal Group. A likely explanation for why this is not the case could relate to the ability to distinguish lineaments, particularly dykes, from their host different rocks. For example, with regards to the topographic domain, the relative lack of lineaments (in the form of dykes) in the dyke-dominated Basal Group could be due to uniform weathering and erosion of outcrops, which then leads to difficulty in discerning individual or sets of dykes at the surface. On the other hand, the contrast in hardness between dykes and host Pillow Lava rocks appears to result in differential erosion and weathering, thus giving dykes an obvious topographic surface expression. Spectrally, it is also difficult to identify individual dykes in host Basal Group rocks because they effectively comprise the same mineralogical composition. Dykes in the Pillow Lavas, however, are more readily recognisable because of the higher spectral contrast linked to their more disparate mineralogical compositions, grain sizes and jointing characteristics. Likewise, lineaments that correspond to faults are usually easier to trace in the Pillow Lavas than in the Basal Group rocks (Gass 1960).

Lineament density maps can also be used to help determine whether lineament maps with greater abundances of lineaments actually contain more information than those with less. If two lineament density maps with considerably different lineament abundances exhibit a strong correlation, then they can essentially be regarded as equivalent, whereas weak correlation suggests that the two maps do indeed contain different information (Parsons and Yearly 1986). The results of the correlation analysis show strong correlations between all lineament density maps (Table 3). Lineament density maps for the Laplacian-filtered ATM PC FCC and Top Hat-transformed LiDAR DTM enhancement techniques are the most weakly correlated, whereas the Laplacian-filtered ATM PC FCC map and the Top Hat-transformed ATM map are the most correlated. Correlation coefficients between the map with the greatest abundance of lineaments (the Laplacian-filtered DTM) and all other maps do not fall below 0.81. This result suggests that all lineament maps essentially contain the same information regardless of the variation in lineament abundance. Also, the results appear to suggest that the additional lineaments identified in the Laplacian-filtered LiDAR DTM are not related to the segmentation of longer lineaments, since higher lineament densities in the affected areas would likely result in somewhat lower correlations than those observed here.

Significance of structural trends and implications

Field-based structural measurements collected along the 4 km transect through the study area show that dykes primarily dip to the NE. This finding is in agreement with the placement of the study area on the western flank of the Larnaca graben proposed by Varga and Moores (1985). The prevailing NW–SE trend revealed by field-based structural measurements is consistent with that expected for an extensional setting. Although dykes appear to dictate this trend, an additional contribution also originates from normal faulting during graben development and dyke injection (Gass 1960). Whilst there is a slight indication of dyke-parallel faulting in the field-based data, the rather variable orientations of the faults recorded along the transect most likely reflect local deformation and possibly younger faulting subsequent to initial formation of the ophiolitic crust. The secondary N-S trend apparent in the field-based data is consistent with a later stage of faulting previously reported in the vicinity of the study area (Gass 1960; Boyle and Robertson 1984).

The main NW–SE and N-S structural trends observed in the study area are also reciprocated in lineament maps generated using the enhanced airborne LiDAR and ATM products. Moreover, these lineament maps are able to resolve structural information in much greater spatial detail than the existing geological maps of the study area. These findings are important because they demonstrate that high-resolution remotely sensed datasets can be used to complement field-based structural mapping. Specifically, when used in conjunction with field-based mapping, airborne datasets clearly offer the potential to help make detailed and comprehensive structural mapping a more time- and cost-efficient process.

Obtained using a combined remote sensing–fieldwork structural mapping approach, our results reveal that there is a fundamental NW-trending steep structural grain wherever the ophiolitic rocks crop out. Based on this, it is also likely that this structural grain exists in surrounding areas under the Lefkara Formation and alluvial–colluvial cover. This fundamental structural grain was found to be dominated by parallel individual dykes and dyke swarms and less abundant normal faults. Otherwise, the hummocky Pillow Lava terrain is characterised by diverse erupted sequences that are complexly stacked and overlapping without other major cross-cutting tectonic structures (Fig. 3a). The NW–SE structural fabric identified in the Pillow Lava and Basal Group rocks and interpreted to occur under sedimentary cover elsewhere in the study area, may be an important consideration for future resource exploration efforts. This is because deep and steep faults and fractured dyke margins may host groundwater, and because major normal faults may have originally been hydrothermal fluid pathways and therefore potential sites of massive sulphide (copper) mineralisation (Fig. 3c, d). Another major implication of this study is that the methods presented can be readily utilised to map dyke and fault trends in greater detail across the ophiolite. Ultimately, this may help to better elucidate the spreading structure of the Troodos ophiolite.

Conclusions

This study investigates the efficacy of high-resolution airborne LiDAR topographic data and ATM imagery for assisting detailed structural mapping of the vegetated ophiolitic rocks and sedimentary cover in an upper section of the Troodos ophiolite. To the best of our knowledge, this is the first attempt to apply airborne LiDAR to detailed structural mapping of ophiolitic rocks. Despite widespread vegetation cover, a preliminary analysis showed that the main structural features — dykes and faults — were recognisable in both the 4 m airborne LiDAR-derived DTM and 4 m ATM imagery as lineaments defined by edges. Accordingly, several different edge enhancement techniques were applied to the datasets in an attempt to augment the visual identification and mapping of lineaments. The resulting lineament maps present structural information in much greater spatial detail than the existing geological maps of the study area. Moreover, the predominant strike trends of lineaments in all maps were found to be consistent with field-based structural data acquired along a transect, in addition to other observations made by ourselves and other workers in the vicinity. The dominant trend in the study area is orientated NW–SE and corresponds at first-order to the direction of dykes injections and extensional faulting associated with the spreading axis of the proposed palaeo-Larnaca graben system. Overall, the results of this study demonstrate the significant potential to produce detailed and comprehensive structural maps efficiently, by using airborne LiDAR data or airborne spectral imagery in conjunction with field-based mapping.

Whilst the results of this study have direct relevance to structural mapping of the Troodos ophiolite and other ophiolites, it is anticipated that high-resolution airborne LiDAR data and airborne spectral imagery can be readily used to augment detailed structural mapping in other settings with a similar Mediterranean climate and vegetation cover. In fact, with the capability of acquiring high-resolution topographic data in densely forested terrain, airborne LiDAR clearly has the potential to be a valuable tool for many aspects of structural mapping in any geological setting, irrespective of vegetation cover. However, the efficacy of airborne LiDAR will be dependent on the generation of an adequate DTM. In densely forested terrain this may require a high LiDAR point density to help maximise the number of ground returns. Conversely, airborne spectral imagery is likely to be of limited use in areas where structural features are subtly expressed in the terrain beneath tall dense vegetation cover.

Although accurate and detailed structural mapping using a manual approach was not time-consuming in this case, automated lineament extraction algorithms would be more efficient for larger map areas. In this respect, further research is required to help improve differentiation between lineaments of a geological origin and lineaments of non-geological significance. An integrated spectral–topographic approach which combines diagnostic morphometric and spectral characteristics could offer additional discriminatory power to help reduce this confusion.

Acknowledgements This work was primarily supported through a Natural Environment Research Council (NERC) CASE Studentship (NE/F00673X/1) in collaboration with the British Geological Survey (BGS) University Funding Initiative, awarded to SG. We gratefully acknowledge the NERC Airborne Research and Survey Facility (grant MC04/30) for data acquisition and the Unit for Landscape Modelling for data pre-processing. We would also like to express our gratitude to the Geological Survey Department of Cyprus (GSD) for providing the digital geological maps, to Dr. Stelios Nicolaides (GSD) and Dr. Simon Jowitt (Monash University) for invaluable logistical and scientific help in the field, and to Luke Bateson (BGS) and Professor Danny Donoghue (Durham University) for AZGCORR and TerraScan software support, respectively. Professor Richard Allmendinger (Cornell University) is also thanked for providing free access to the Stereonet/StereoWin software. SG is grateful to the Geological Remote Sensing Group for receipt of a Student Fieldwork and Travel Award. JN publishes with permission of the Executive Director, British Geological Survey (NERC). We thank Dr. Terry Pavlis and an anonymous reviewer for their comments and suggestions which helped to improve the quality of this manuscript.

References

Ali SA, Pirasteh S (2004) Geological applications of Landsat Enhanced Thematic Mapper (ETM) data and Geographic Information System (GIS): mapping and structural interpretation in south-west Iran, Zagros Structural Belt. Int J Remote Sens 25:4715–4727

Argialas DP, Mavrantza OD (2004) Comparison of edge detection and Hough transform techniques for the extraction of geologic features. Int Arch Photogramm Remote Sens Spat Inf Sci 34:790–795

Arrowsmith JR, Zielke O (2009) Tectonic geomorphology of the San Andreas Fault zone from high resolution topography: An example from the Cholame segment. Geomorphology 113:70–81

Axelsson P (2000) DEM Generation from Laser Scanner Data Using Adaptive TIN Models. Int Arch Photogramm Remote Sens 33:110–117

Barnes JW, Lisle RJ (2004) Basic Geological Mapping, Fourth edition. John Wiley and Sons, Chichester

Bear LM (1960) The geology and mineral resources of the Akaki-Lythrodondha area, Memoir 3. Geological Survey Department, Cyprus

Boyle JF, Robertson AHF (1984) Evolving metallogenesis at the Troodos spreading axis. Geol Soc Lon Spec Publ 13:169–181

Corgne S, Magagi R, Yergeau M, Sylla D (2010) An integrated approach to hydro-geological lineament mapping of a semi-arid region of West Africa using Radarsat-1 and GIS. Remote Sens Environ 114:1863–1875

Cunningham D, Grebby S, Tansey K, Gosar A, Kastelic V (2006) Application of airborne LiDAR to mapping seismogenic faults in forested mountainous terrain, southeastern Alps, Slovenia. Geophys Res Lett 33:L20308

Fitton NC, Cox SJD (1998) Optimising the application of the Hough transform for automatic feature extraction from geoscientific images. Comput Geosci 24:933–951

Gass IG (1960) The geology and mineral resources of the Dhali area, Memoir 4. Geological Survey Department, Cyprus

Gass IG (1968) Is the Troodos massif of Cyprus a fragment of Mesozoic ocean crust? Nature 220:39–42

Grebby S, Cunningham D, Naden J, Tansey K (2010) Lithological mapping of the Troodos ophiolite, Cyprus, using airborne LiDAR topographic data. Remote Sens Environ 114:713–724

Grebby S, Naden J, Cunningham D, Tansey K (2011) Integrating airborne multispectral imagery and airborne LiDAR data for enhanced lithological mapping in vegetated terrain. Remote Sens Environ 115:214–226

Harding DJ, Berghoff GS (2000) Fault scarp detection beneath dense vegetation cover: airborne lidar mapping of the Seattle fault zone, Bainbridge Island, Washington State. In: Proceedings of the American Society of Photogrammetry and Remote Sensing Annual Conference, Washington D.C., May 2000. American Society of Photogrammetry and Remote Sensing, Bethesda, Maryland

Haugerud RA, Harding DJ, Johnson SY, Harless JL, Weaver CS, Sherrod BL (2003) High-resolution Lidar topography of the Puget Lowland, Washington — A bonanza for earth science. GSA Today 13:4–10

Hill RA, Wilson AK, George M, Hinsley SA (2010) Mapping tree species in temperate deciduous woodland using time-series multi-spectral data. Appl Veg Sci 13:86–99

Jensen JR (2005) Introductory digital image processing: a remote sensing perspective. Prentice Hall, New Jersey

Jordan G, Schott B (2005) Application of wavelet analysis to the study of spatial pattern of morphotectonic lineaments in digital terrain models. A case study. Remote Sens Environ 94:31–38

Karnieli A, Meisels A, Fisher L, Arkin Y (1996) Automatic extraction and evaluation of geological linear features from digital remote sensing data using a Hough transform. Photogramm Eng Remote Sens 62:525–531

Koike K, Nagano S, Kawaba K (1998) Construction and analysis of interpreted fracture planes through combination of satellite-image derived lineaments and digital elevation model data. Comput Geosci 24:573–583

Koike K, Nagano S, Ohmi M (1995) Lineament analysis of satellite images using a Segment Tracing Algorithm (STA). Comput Geosci 21:1091–1104

Kraus K, Pfeifer N (1998) Determination of terrain models in wooded areas with airborne laser scanner data. ISPRS J Photogramm Remote Sens 53:193–203

Kresic N (1995) Remote sensing of tectonic fabric controlling groundwater flow in Dinaric Karst. Remote Sens Environ 53:85–90

Masoud A, Koike K (2006) Tectonic architecture through Landsat-7 ETM+/SRTM DEM-derived lineaments and relationship to the hydrogeologic setting in Siwa region, NW Egypt. J Afr Earth Sci 45:467–477

Moore GK, Waltz FA (1983) Objective procedures for lineament enhancement and extraction. Photogramm Eng Remote Sens 49:641–647

Moores EM, Vine FJ (1971) Troodos Massif, Cyprus and other ophiolites as oceanic crust: evaluation and implications. Philos T Roy Soc A 268:443–467

Mountrakis D, Pavlides S, Zouros N, Astaras T, Chatzipetros A (1998) Seismic fault geometry and kinematics of the 13 May 1995 Western Macedonia (Greece) earthquake. J Geodyn 26:175–196

Nyborg M, Berglund, J., Triumf C-A (2007) Detection of lineaments using airborne laser scanning technology: Laxemar-Simpevarp, Sweden. Hydrogeol J 15:29–32

O'Leary DW, Friedman JD, Pohn HA (1976) Lineament, linear, lineation - some proposed new standards for old terms. Geol Soc Am Bull 87:1463–1469

Parsons AJ, Yearley, R J (1986) An analysis of geologic lineaments seen on LANDSAT MSS imagery. Int J Remote Sens 7:1773–1782

Pavlis TL, Bruhn RL (2011) Application of LIDAR to resolving bedrock structure in areas of poor exposure: An example from the STEEP study area, southern Alaska. Geol Soc Am Bull 123:206–217

Peña SA, Abdelsalam MG (2006) Orbital remote sensing for geological mapping in southern Tunisia: Implication for oil and gas exploration. J Afr Earth Sci 44:203-219

Prentice CS, Crosby CJ, Harding DJ, Haugerud RA, Merritts DJ, Gardner TW, Koehler RD, Baldwin JN (2003) Northern California LIDAR data: A tool for mapping the San Andreas Fault and pleistocene marine terraces in heavily vegetated terrain. Paper presented at American Geophysical Union Fall Meeting, San Francisco, California, December 2003

Qari MYHT (1991) Application of Landsat TM data to geological studies, Al-Khabt Area, Southern Arabian Shield. Photogramm Eng Remote Sens 57:421–429

Ricchetti E, Palombella, M (2005) Application of Landsat 7 ETM+ imagery for geological lineament analysis of Southern Italy. In: Proceedings of IGARSS 2005, Geoscience and Remote Sensing Symposium, Seoul, South Korea, July 2005. IEEE International

Saha AK, Gupta, RP, Arora MK (2002) GIS-based landslide hazard zonation in the Bhagirathi (Ganga) Valley, Himalayas. Int J Remote Sens 23:357–369

Süzen ML, Toprak V (1998) Filtering of satellite images in geological lineament analyses: an application to a fault zone in Central Turkey. Int J Remote Sens 19:1101–1114

Tripathi NK, Gokhale KVGK, Siddiqui MU (2000) Directional morphological image transforms for lineament extraction from remotely sensed images. Int J Remote Sens 21:3281–3292

Varga RJ, Moores EM (1985) Spreading structure of the Troodos ophiolite, Cyprus. Geology 13:846–850

Wallace J, Morris B, Howarth P (2006) Identifying structural trend with fractal dimension and topography. Geology 34:901–904

Wladis D (1999) Automatic lineament detection using digital elevation models with second derivative filters. Photogramm Eng Remote Sens 65:453–458

Figure captions

Fig. 1. a Location and geology (at 1:31,680- and 1:250,000-scale) of the Troodos ophiolite and the study area. **b** Shaded relief model of the study area generated from the 4 m airborne LiDAR DTM. **c** A red-green-blue true-colour composite image of the study area generating using bands 5, 3, and 2 of the 4 m ATM imagery. Labels A, B and C in **b** and **c** indicate the locations of the example fault, dyke and fault ridge shown in Fig. 4a, d and Fig. 3b, respectively. Red shading in **b** and **c** depicts transect along which field-based structural data were acquired. Digital geology provided by the Cyprus Geological Survey Department.

Fig. 2. Field photographs showing typical examples of structural features observed in the study area. **a** Set of NW-SE striking dykes intruding Pillow Lavas; **b** and **c** brittle fault zones in Pillow Lavas; **d** NW-SE trending dykes expressed in the landscape; **e** and **f** upstanding dykes intruding Pillow Lavas.

Fig. 3. Important geological features of the study area. **a** Typical hummocky Pillow Lava landscape comprising stacks of erupted lavas devoid of steep structures; **b** upstanding silicified strike-slip fault zone which was assumed to be a dyke prior to field verification (location C in Fig. 1b); **c** parallel dyke swarm with abundant dyke margin-parallel fractures; **d** gossan alteration within Pillow Lavas and along dyke margins and joints.

Fig. 4. Expression of the main types of structural features in the remotely sensed data. **a** Field photograph of the example fault at location A in Fig. 1b, c, and cross-sectional profiles showing the expression of this fault cleft as a trough in **b** the airborne LiDAR DTM and **c** ATM Band 2 image. **d** Field photograph of the example dyke(s) at location B in Fig. 1b, c, and cross-sectional profiles showing the expression of the dyke(s) as a ridge in **e** the airborne LiDAR DTM and **f** ATM Band 5 image.

Fig. 5. Weighting structure of the 3×3 pixel kernel used in Laplacian filtering.

Fig. 6. Structural data obtained through field-based mapping along the transect indicated in Fig. 1b, c. **a** Equal-area stereonet plot revealing a dominant NW-SE trend and steep NE dip for 64 dykes observed in the field. **b** Equal-area stereonet plot showing the variable strike and dip for 16 faults mapped in the field. **c** Equal-area stereonet contour plot of poles to planes for the combined dyke and fault data (shown in **a** and **b**, respectively) reveals a dominant NW-SE structural trend within the study area.

Fig. 7. Lineament maps and rose diagrams (inset) generated through visual interpretation of **a** LiDAR shaded relief model (15%), **b** ATM PC FCC (17%), **c** Top Hat-transformed LiDAR DTM (12%), **d** Top Hat-transformed ATM PC FCC (12%), **e** Laplacian-filtered LiDAR DTM (16%) and **f** Laplacian-filtered ATM PC FCC (16%). Bracketed percentages denote proportion of lineaments represented by outer circle in corresponding rose diagrams (see Table 2 for total number of lineaments in each map). Average orientations are indicated on rose diagrams.

Fig. 8. Frequency distributions of lineament lengths mapped using the various enhanced data products. **a** LiDAR shaded relief model; **b** ATM PC FCC; **c** Top Hat-transformed LiDAR DTM; **d** Top Hat-transformed ATM PC FCC; **e** Laplacian-filtered LiDAR DTM; **f** Laplacian-filtered ATM PC FCC.

Fig. 9. Lineament density maps derived from lineament maps generated through visual interpretation of **a** LiDAR shaded relief model, **b** ATM PC FCC, **c** Top Hat-transformed LiDAR DTM, **d** Top Hat-transformed ATM PC FCC, **e** Laplacian-filtered LiDAR DTM and **f** Laplacian-filtered ATM PC FCC. Shading represents low (white) to high (black) lineament density.

Table 1. Eigenvalues and eigenvector loadings for the first three PC bands derived from the application of PCA to ATM Bands 2–10.

Eigenvectors	PC1	PC2	PC3
ATM 2	0.33	-0.40	-0.19
ATM 3	0.35	-0.32	-0.20
ATM 4	0.35	-0.26	-0.16
ATM 5	0.36	-0.17	-0.14
ATM 6	0.36	0.19	-0.19
ATM 7	0.33	0.47	-0.19
ATM 8	0.30	0.57	-0.05
ATM 9	0.32	0.17	0.50
ATM 10	0.29	-0.19	0.74
Eigenvalues	7.25	1.00	0.53
Variance (%)	80.56	11.10	5.84
Cumulative variance (%)	80.56	91.66	97.50

Table 2. Statistics relating to the abundance and lengths of lineaments identified using the various enhancement techniques.

Enhancement technique	Number of lineaments	Min. length (m)	Max. length (m)	Average length (m)	Total length (m)
LiDAR shaded relief model	192	51.1	801.0	207.4	39,817.5
ATM PC FCC	227	38.2	714.7	167.5	38,021.0
Top Hat-transformed LiDAR DTM	199	55.2	709.2	199.5	39,707.1
Top Hat-transformed ATM PC FCC	210	52.5	665.4	217.0	45,563.1
Laplacian-filtered LiDAR DTM	316	37.7	735.1	158.4	50,059.3
Laplacian-filtered ATM PC FCC	239	53.5	868.3	174.9	41,791.4

Table 3. Correlation matrix for the lineament density maps.

	LiDAR shaded relief model	ATM PC FCC	Top Hat-transformed LiDAR DTM	Top Hat-transformed ATM PC FCC	Laplacian-filtered LiDAR DTM	Laplacian-filtered ATM PC FCC
LiDAR shaded relief model	–					
ATM PC FCC	0.82	–				
Top Hat-transformed LiDAR DTM	0.89	0.79	–			
Top Hat-transformed ATM PC FCC	0.87	0.87	0.83	–		
Laplacian-filtered LiDAR DTM	0.88	0.81	0.84	0.85	–	
Laplacian-filtered ATM PC FCC	0.81	0.87	0.76	0.90	0.81	–

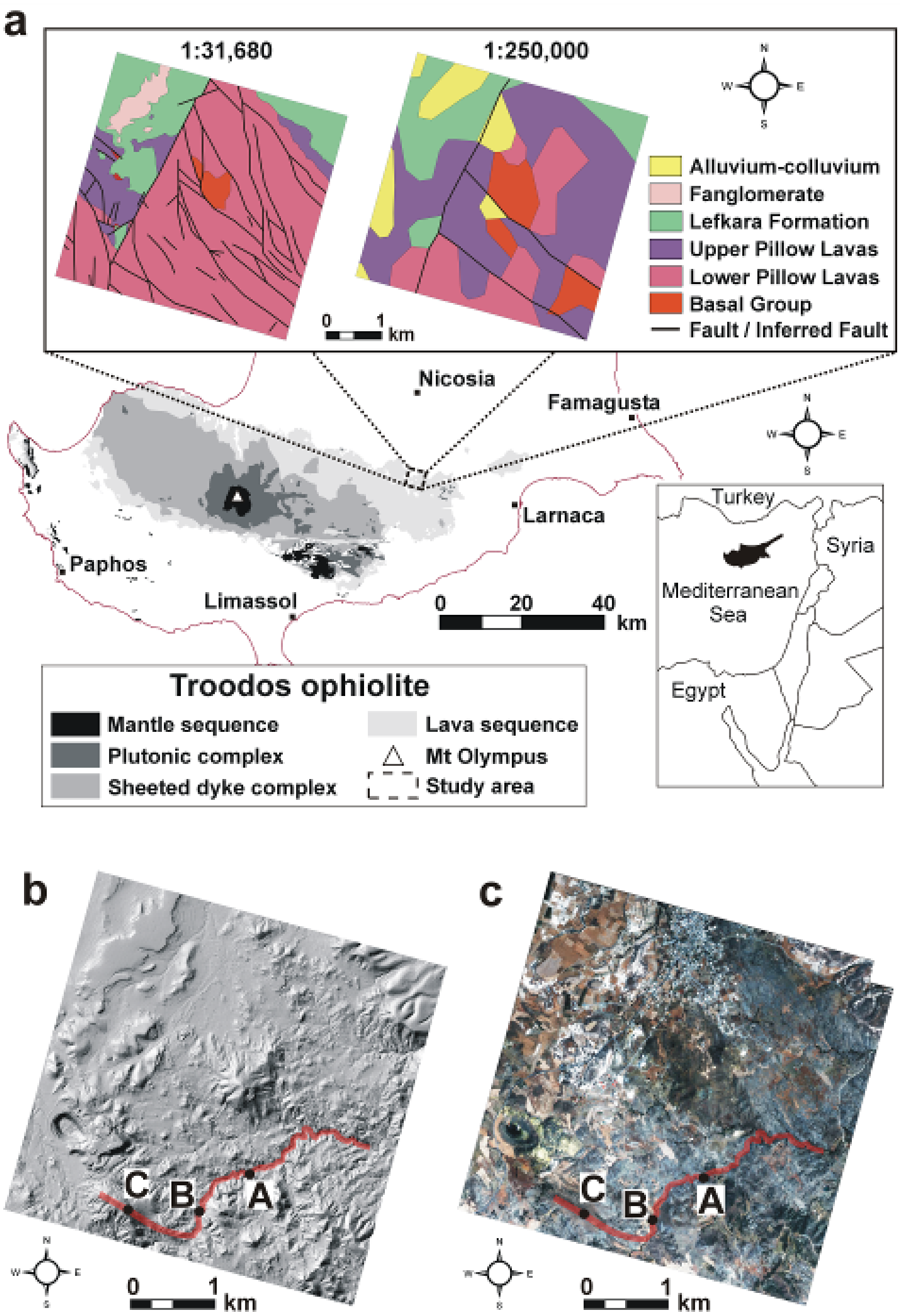
a
1:31,680
1:250,000
Alluvium-colluvium
Fanglomerate
Lefkara Formation
Upper Pillow Lavas
Lower Pillow Lavas
Basal Group
Fault / Inferred Fault
0 1 km
Nicosia
Famagusta
Larnaca
Paphos
Limassol
0 20 40 km
Turkey
Syria
Mediterranean Sea
Egypt
Troodos ophiolite
Mantle sequence
Plutonic complex
Sheeted dyke complex
Lava sequence
Mt Olympus
Study area
b
c
A
B
C
0 1 km

FIG.1

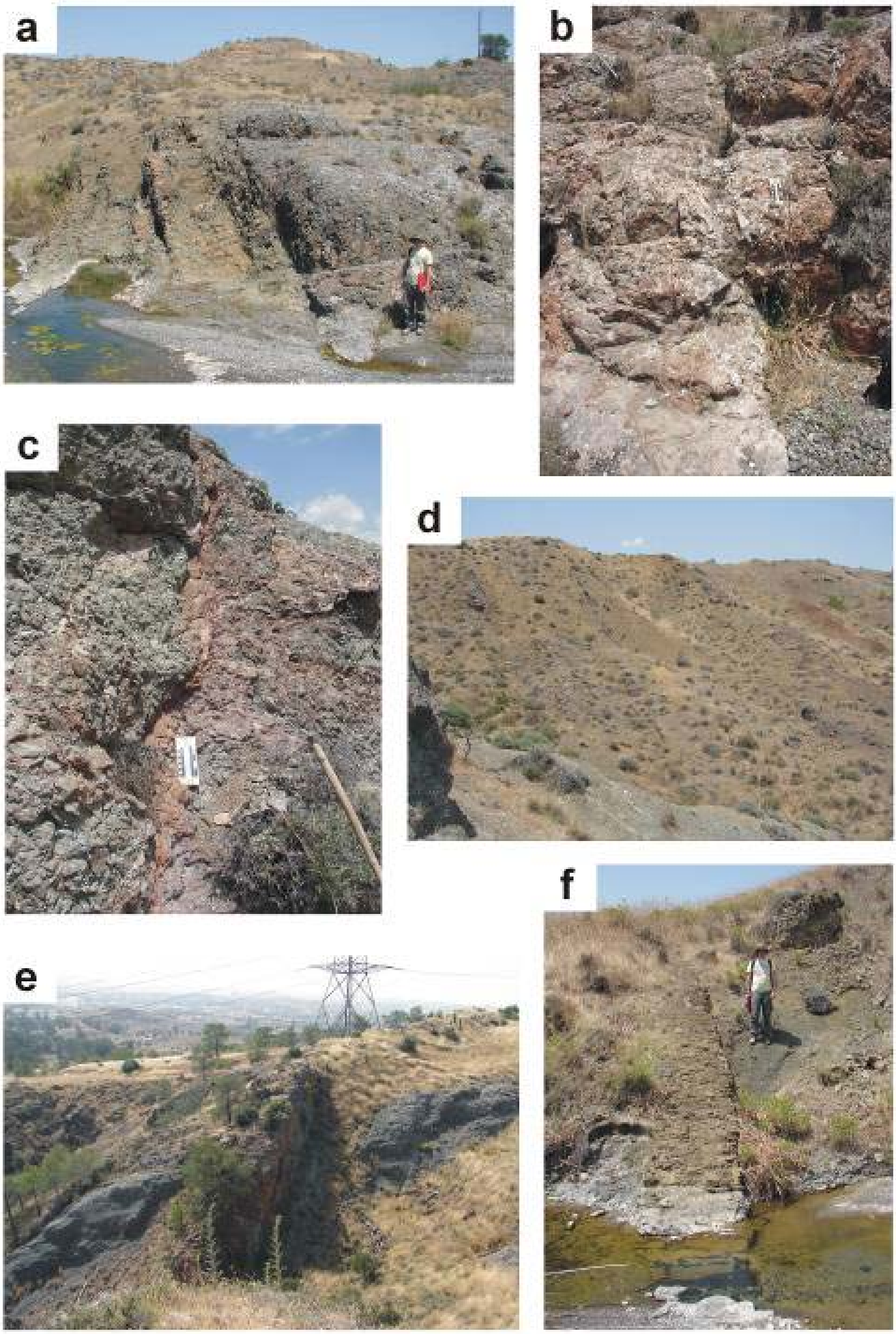

Fig.2

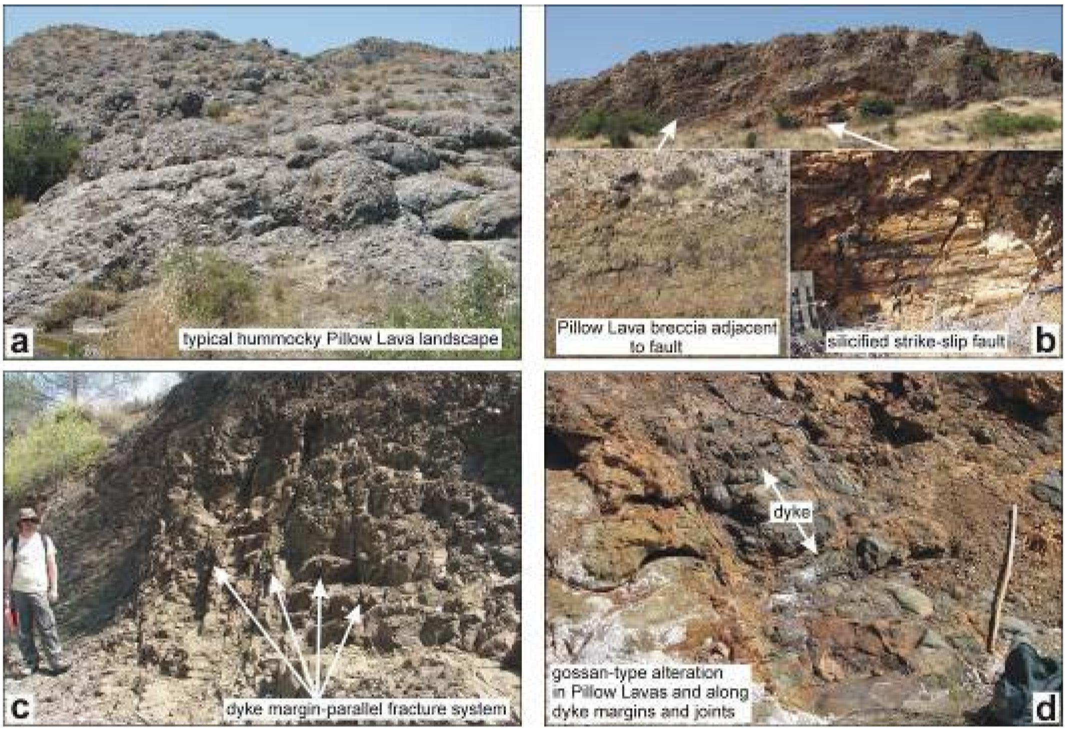
typical hummocky Pillow Lava landscape
a
Pillow Lava breccia adjacent to fault
silicified strike-slip fault
b
c
dyke margin-parallel fracture system
dyke
gossan-type alteration in Pillow Lavas and along dyke margins and joints
d

Fig. 3

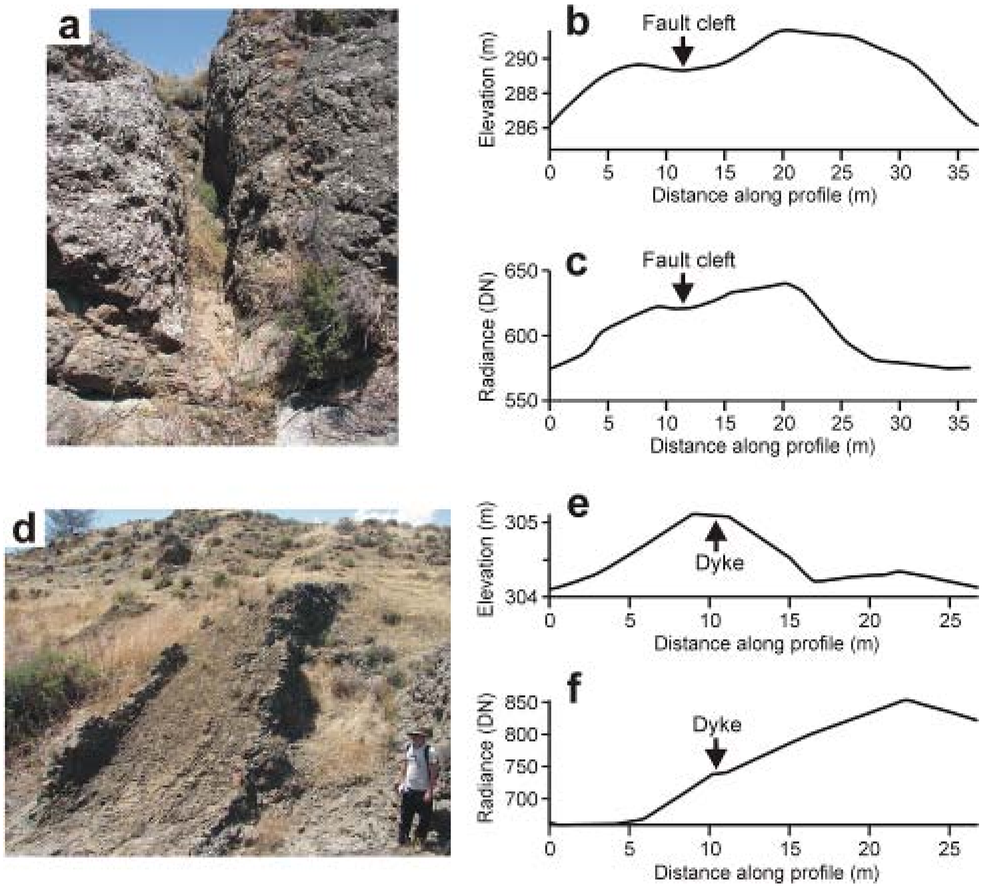

Fig. 4

0	-1	0
-1	4	-1
0	-1	0

Fig. 5

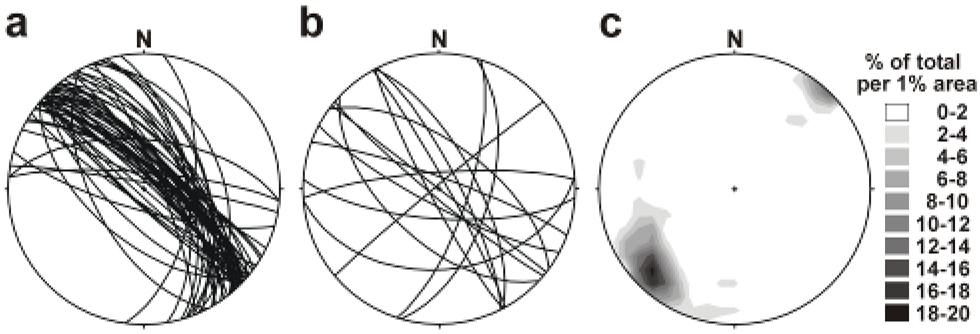

Fig. 6

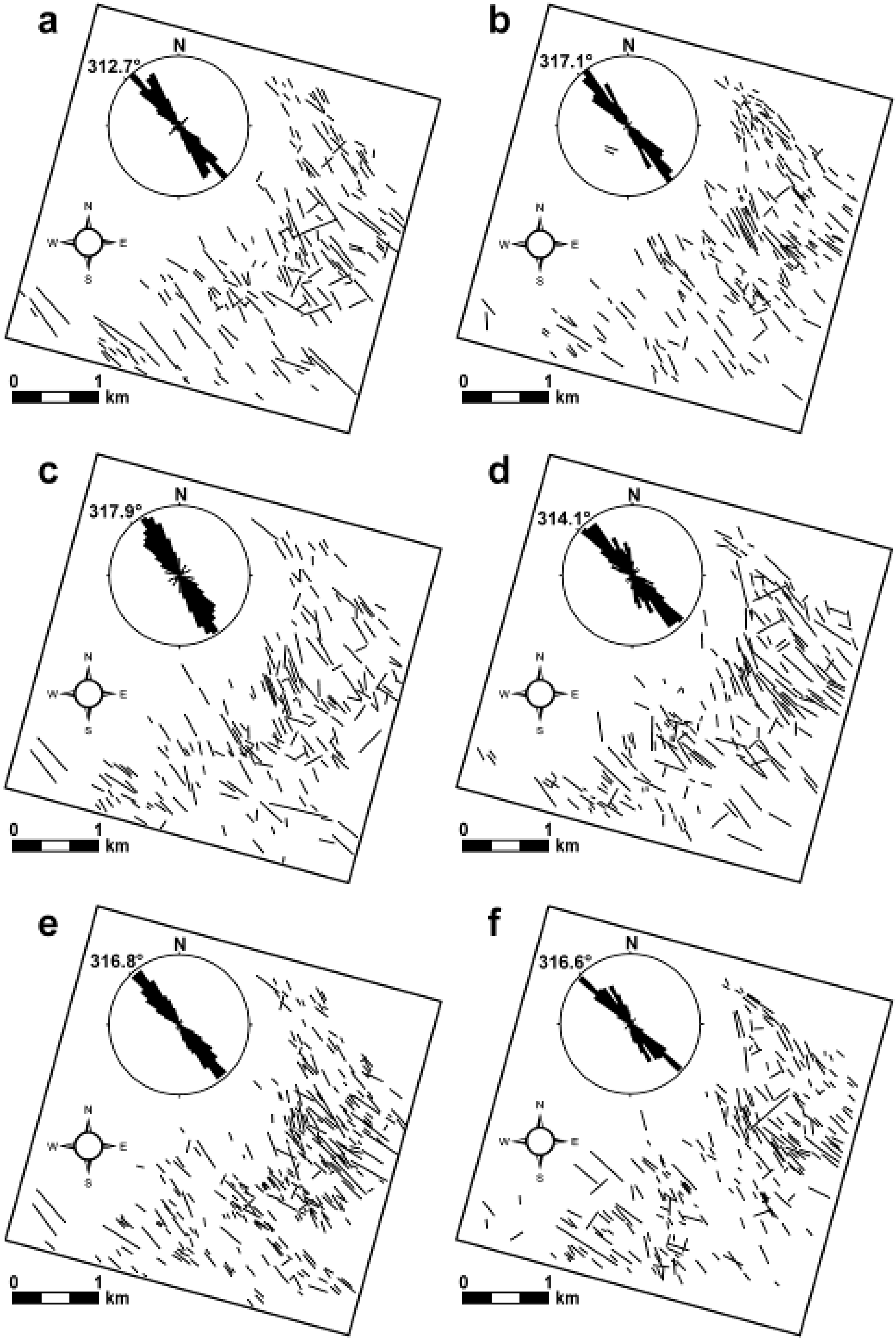

Fig.7

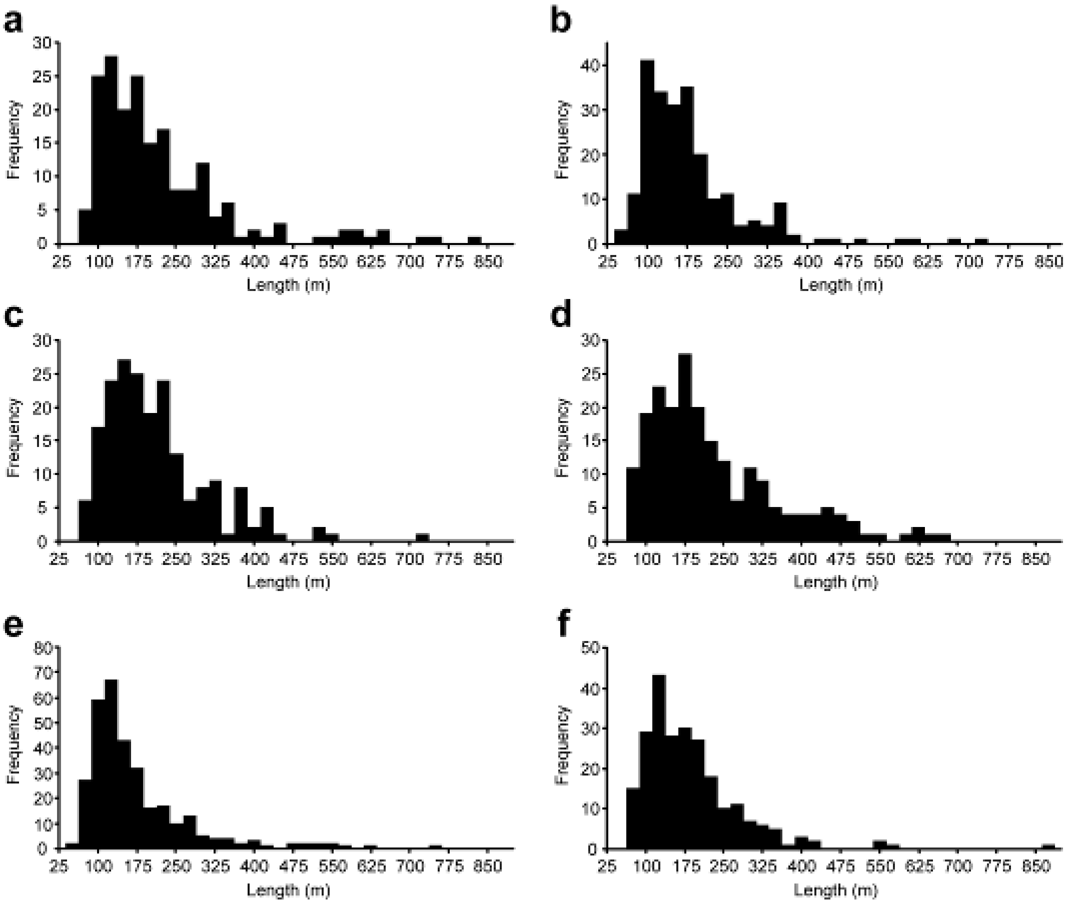
a
b
c
d
e
f
Frequency
Length (m)
25 100 175 250 325 400 475 550 625 700 775 850

Fig. 8

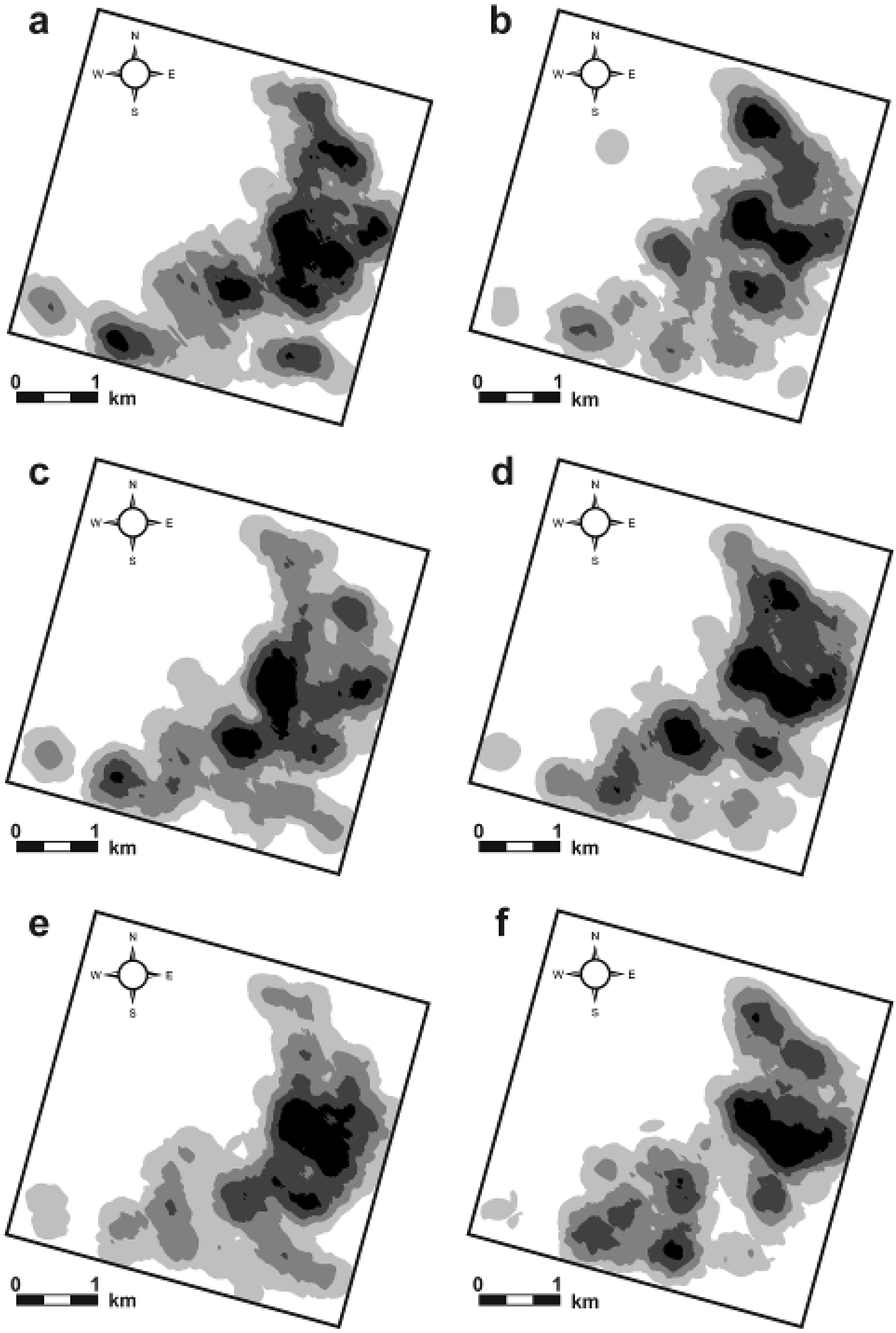

Fig. 9